FRETTING–FATIGUE BEHAVIOR OF BOLTED JOINTS USING FEM METHOD

Sehoul Mohamed[1], Benguediab Mohamed[1,*], Kettaf Fatima Zohra[1], Benhamena Ali[2]

[1] Laboratory of Materials and Reactive Systems, Department of Mechanical Engineering,University of Sidi Bel Abbes, Algeria.
[2] Department of Mechanical Engineering, University of Mascara, Algeria.

*corresponding author: e-mail: benguediab_m@yahoo.fr

Resume

In this paper, the fretting damage of a mechanical bolted assembly in three dimensions is studied using a numerical approach. The study consist to analyze the cylindrical coordinates in stress fields and other fretting parameters depending on the angle and radius of the contact areas, and also to determine the position of the initiation and propagation of the crack.

The numerical simulation is done in 3D in order to better describe the real behavior in fretting of a bolted joint. According to the simulation results, the tightening torque plays a significant role in the load transfer. The results allowed us to determine the stress that triggers the initiation and crack propagation, and locate the damaged area by fretting.

Article info

Article history:
Received 24 January 2017
Accepted 03 March 2017
Online 05 December 2017

Keywords:
Fretting;
Bolted assembly;
Numerical approach;
Damage area

Available online: http://fstroj.uniza.sk/journal-mi/PDF/2017/05-2017.pdf

ISSN 1335-0803 (print version)
ISSN 1338-6174 (online version)

1. Introduction

Fretting is a special wear process that occurs at the contact area between two materials under load and subject to minute relative motion by vibration or some other force[1]. This phenomenon has been recognized and studied for along time. It was reported first by Eden et al. in 1911 [2], but it wasn't well understood until 1927 when studied by Tomlinson [3].

Fretting damage is differentiated by three distinct modes: it can occur as a result of fretting wear [4 - 6]; which happens for relatively small vibratory or cyclic motion, normally results in relatively little damage and rarely causes premature structural failure; or as gross sliding wear [7 - 9], which occurs for relatively large vibratory motion, normally results in visual surface damage, but rarely causes premature structural failure; or fretting fatigue - this term is used to describe situations where microslip between contacting surfaces appears to give rise to a reduction in fatigue life when compared to a plain component. This third mode leads to catastrophic failure [10]. Due to its importance and the damage it can cause, the study of this phenomenon in its three configurations is very necessary.

Fretting fatigue is a combination of two complex phenomenon's. There are a lot of practical applications that are subjected to fretting fatigue. Based on contact conditions, e.g. surface finish, coefficient of friction, etc, and mechanical variables, e.g. axial stress, contact stress and slip amplitude, fretting damage at contact interface can cause crack initiation and growth leading to catastrophic and sudden fracture. Experimental studies of fretting fatigue have taken different forms: Bridge type [11], Single clamp type pad [12 - 14], and Single and Double Bolted Lap Joint [15 - 17].

The finite element method (FEM) is a numerical technique for finding approximate solutions to boundary value problems. It is very popular and useful for analyzing fretting fatigue behavior [18 - 26]. In most studies we can observe that the fretting fatigue life decreases with the increase of contact forces.

This paper adopts the 3D-FEM technique to predict the most dangerous strain that causes the initiation and propagation of crack, and determine the damaged area by fretting. We consider a double joint cover assembly bolted with only a single bolt, we introduce a torque per revolution of the nut by an angle θ of 106.6°, and we consider a friction between the contact surfaces (μ=0.2), we observe that the intensity of the torque leads to the augmentation of equivalent Von Mises stresses, shear stresses, and causes the increase of the normal stress between the plates.

2. Description of the Problem

The geometry of the bolted assembly and different boundary conditions used in the finite-element analysis are described in the following:

2.1 Geometry

Fig. 1 shows the geometry of three bolted rectangular plates with length l = 160 mm, width w = 25 mm, and thickness t = 3.2 mm.

2.2 Material

The aluminum alloy 7075-T6 plates are used in this case. Its properties are taken from Military Handbook 5H [28] and are shown in the Table 1.

The material for the bolt is high-strength and high grade alloy steel (AJAX Steel Bolt Class 8.8 and UNBRAKO Steel Bolt Class 12.8). Typical Young’s modulus and Poisson’s ratio for this material are 210,000 MPa and 0.3 respectively [28].

2.3 Boundary conditions

There are three overlapping plates assembled as shown in Fig. 2, the left sides of the two plates are fixed and the force is applied to the right side of the intermediate plate.

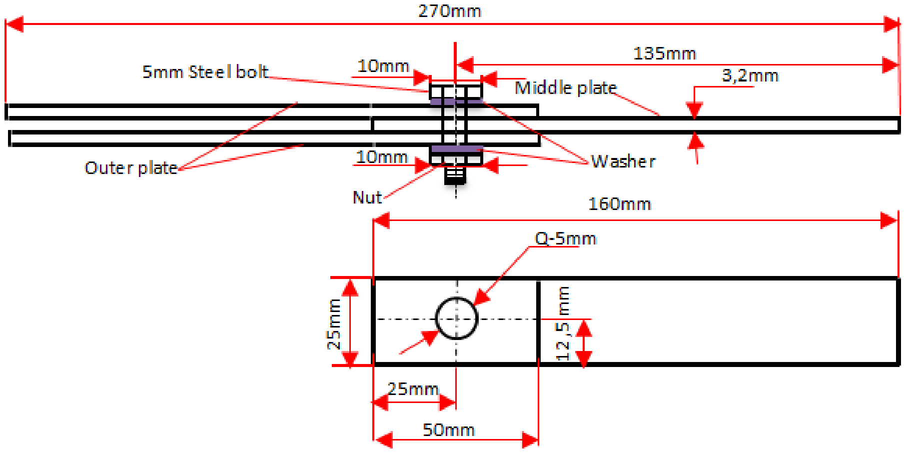

Fig. 1. Bolted assembly in double joint cover [27].
(full colour version available online)

Table 1

Mechanical properties of the aluminum alloy 7075-T6 [28].

Yield Stress σ_E (MPa)	Ultimate Stress σ_u	Young’s Modulus E (MPa)	Poisson’s Ratio ν	Strength Coefficient K (MPa)	Hardening exponent
412	590	71000	0.33	850	0.035

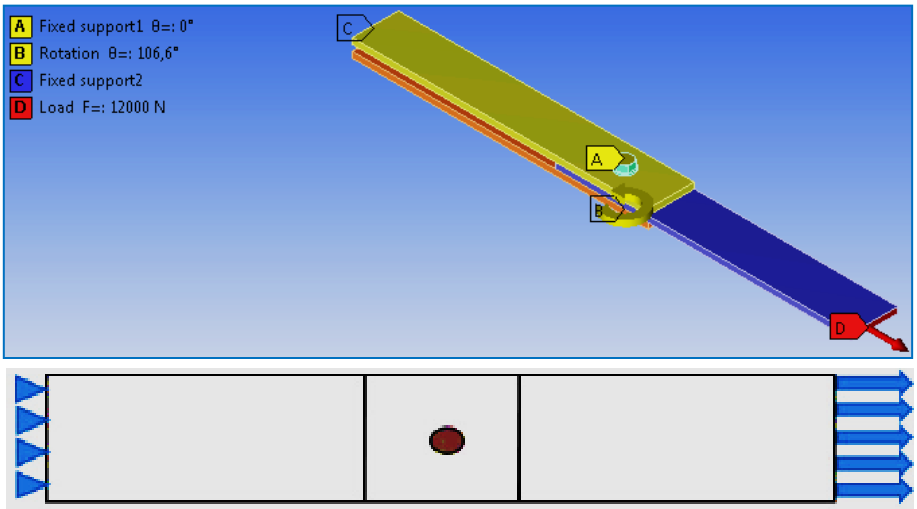

Fig. 2. Boundary conditions and loading condition.
(full colour version available online)

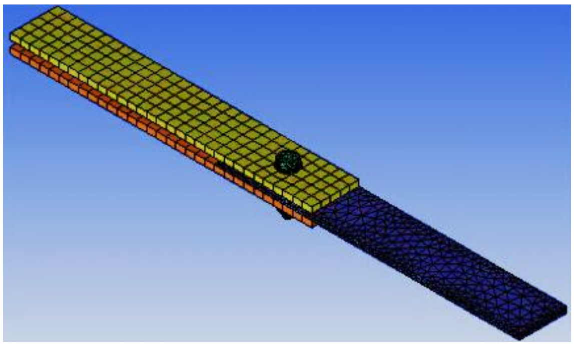

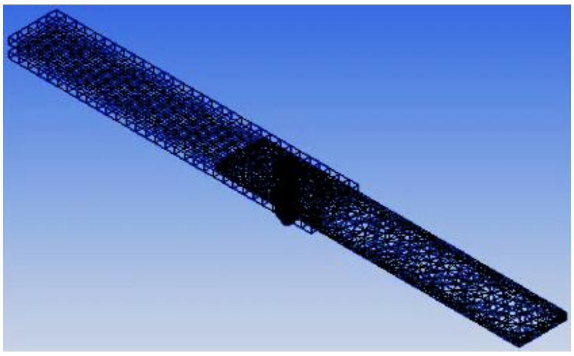

a) full model *b) filaire model*
Fig. 3. Finite elements detail model: Mesh of the bolted assembly.
(full colour version available online)

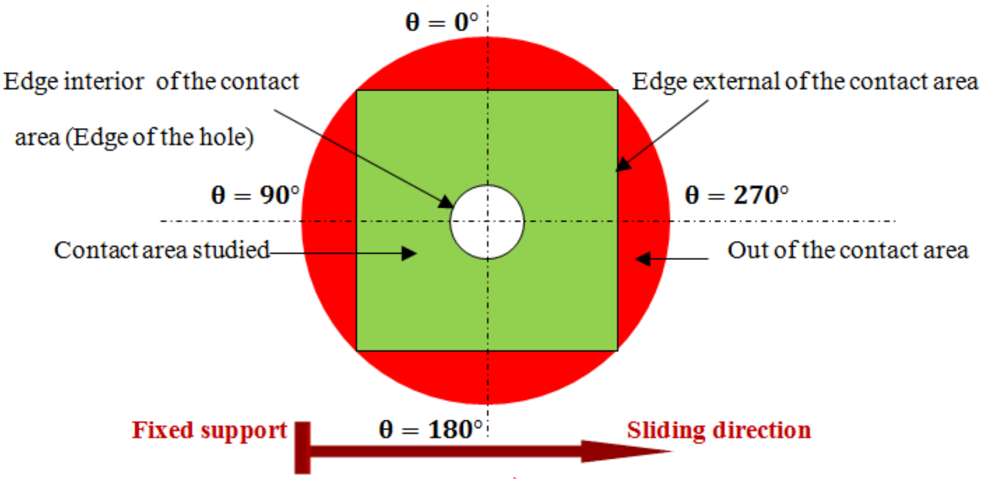

Fig. 4. Representation of the contact area.
(full colour version available online)

3. Finite Element Analysis

Finite element analysis is an important tool to design practical mechanical joints, such as the bolted assemblies. According to the dimensions of the structure, a three dimensional model was generated using the commercial software ANSYS (ANSYS 11, [29]) in order to determine stress field at contact zone.

In this modeling the assembly elements (screws, nuts, lock nuts, and washers) are considered as rigid bodies in the finite element model. The details of the bolted assembly and assembly elements are shown in Fig. 3.

The method used in this modeling to realize the tightening torque is the method of the turn of nut [30]. This method is based on the application of a rotation quantity θ to the nut [30] given by equation (1).

$$\theta = 90° + \Sigma t + d \tag{1}$$

Where: t is the total thickness of the assembled plates in mm and d is the bolt diameter in mm.

3.1The contact area

The contact area Z is comprised between an inner edge in the form of a circle and an outer edge in the form of a square (see Fig. 4).

To define the contact area you must define the following two spaces:

In the Euclidean space (2):

$$\Omega_1 = \left\{ \begin{pmatrix} x \\ y \\ z \end{pmatrix} \in \mathbb{R}^3 \Big/ \begin{matrix} |x| \leq 12.5\ mm \\ |y| \leq 12.5\ mm \\ |z| \leq 1.6\ mm \end{matrix} \right\} \tag{2}$$

The Cylindrical space:

$$\Omega_2 = \left\{ \begin{pmatrix} r \\ \theta \\ z \end{pmatrix} \in \mathbb{R}^3 \Big/ \begin{matrix} 2.5 \leq r \leq 17.67\ mm \\ 0° \leq \theta \leq 360° \\ |z| \leq 1.6\ mm \end{matrix} \right\} \tag{3}$$

$z \notin \Omega_1$ if $y = 0$ and $|x| \leq 2.5$ mm where $x = 0$ and $|y| \leq 2.5$ mm

$z \notin \Omega_2$ if 12.5 mm $\leq r \leq 17.677$ mm and $|\theta| = 90°$ or $\theta = 0°$ or $\theta = 180°$.

3.2 The damage sources

A cyclic load (According to an Euclidean landmark):

$$\vec{F}(KN) = \begin{pmatrix} 0 \\ 0 \\ 12 \end{pmatrix} \tag{4}$$

A tightening torque (In rotational form according to the cylindrical landmark):

$$\vec{C} = \begin{pmatrix} 0 \\ 0 \\ \theta = 106.6° \end{pmatrix} \tag{5}$$

The friction coefficient between the plates $\mu = 0.2$.

4. Results

The aim is summarized in two essential points:

– Determination of the most dangerous stress that triggered the crack initiation and propagation

– Determination of the position of the priming and propagation of crack

Fig. 5 shows the Iso values of the equivalent Von Mises stresses in the contact area on the intermediate aluminum plate alone under the same loading conditions. We note that the value of this constraint is constant $\sigma_{Von\text{-}Mises} = 269.31$ MPa, the distribution is uniform in this area, so it isn't located in a defined position between the hole edge and the edge of the contact area.

In order to better analyze the combined effect of the tightening torque ($\theta = 106.6°$) and the cyclic load (F = 12 KN) on the stress field distribution and correctly locate the crack initiation site in the contact area, a more detailed analysis was carried out of each stress component between the edge of the hole and the edge of the contact area. In the numerical model, an angle serves as a reference to indicate the position for which stresses are calculated (Fig. 6).

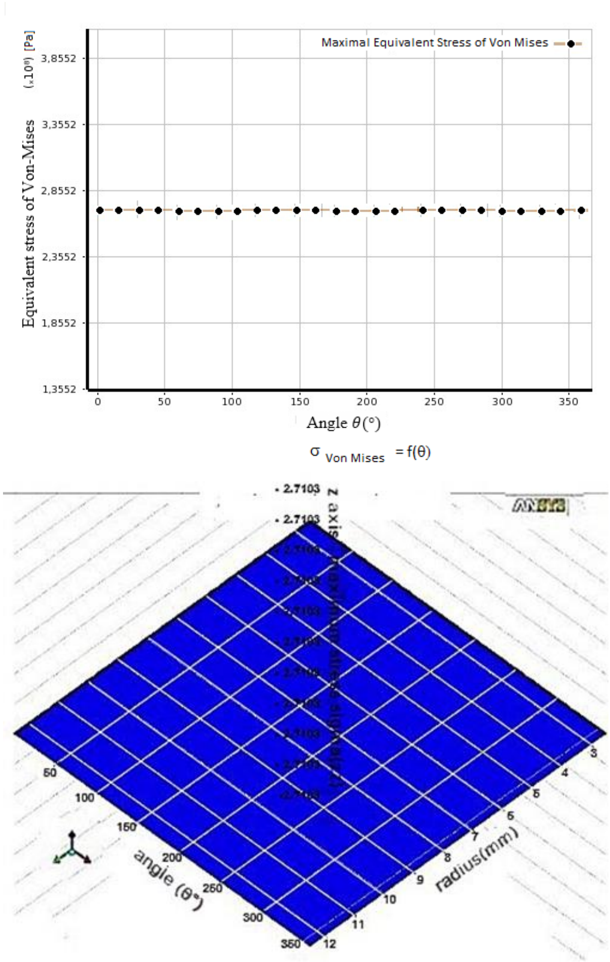

Fig. 5. Distribution of the equivalent Von-Mises stresses between the edge of the hole and the edge of the contact area.
(full colour version available online)

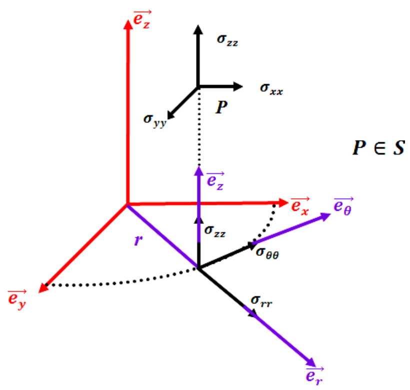

Fig. 6. Appointment of position of a point P in the surface of contact and their stresses generated in the two different cylindrical and Cartesian orientations.
(full colour version available online)

The analysis of the graphs shown in Figs. 7 and 8 reflects a similar behavior as that obtained previously. The only difference is the distribution of the components of shear stresses, and stresses $\sigma_{\theta\theta}$. This aspect can be attributed to the effect of the angular parameter when using the cylindrical coordinates in an axis system. The stress σ_{rr} is varied according to the two coordinates: angle and radius, it takes the maximum value σ_{rr} = 288.94 MPa at the position defined by: (r = 7.5mm; θ = 179.77 °), and the constrained σ_{zz} remains stable and unchanged. By comparing the ranges of this constraint (σ_{rr}) with the other components of the stress field ($\sigma_{\theta\theta}$, σ_{zz}, $\sigma_{r\theta}$,, σ_{θ}, σ_{rz}), we can conclude that the risk of crack initiation and propagation is associated by the stress component (σ_{rr}).

From the numerical analysis we can say that the initiation of the crack in the intermediate plate for this type of loading takes place in a path defined by a radius equal to 7.5 mm and an angle roughly equal to 180°.

In order to better model this behavior, and to give a better justification of the conclusions already found, taking into account the distribution of contact pressure, frictional stress, sliding and penetration is therefore necessary (Fig. 9).

By analyzing the graphs shown in Fig. 9, it can be seen that the values of the contact pressure, the friction stress, and the penetration: P = 22.90 MPa, $\sigma_{friction}$ = 14.29 MPa and pe = 0.91 µm, are maximum at the position defined by θ = 179.61° ≅ 180° compared to those found at the edge of the hole where the radius r =2.5 mm (P = 22.87 MPa, $\sigma_{friction}$= 14.29 MPa, pe = 0.87µm). The evolution of the friction stress is subdivided into three domains: Contact area (red), intermediate area (green) and non-contact area (blue).

The sliding increases gradually with the angle and the radius increase and finally reaches the maximum value g = 65.01 µm at θ = 0 °, r = 2.5 mm or r = 12.5 mm. Then it begins to decrease towards a value g = 61.68 µm at θ = 179.61 °, r = 7.5 mm. The decrease in sliding in the ring domain $6 \leq r \leq 7$ and the increase in the friction stress at $3 \leq r \leq 7$ and the contact pressure at $6 \leq r \leq 11$ in a contact problem can be explained by the phenomenon of adhesion which is justified by penetration. While the sliding phenomenon is the inverse of all that has been observed in adhesion, we can consider the increase of the sliding in the ring domain

$2.5 \leq r \leq 5.61$ and $8.37 \leq r \leq 12.5$ as an adhesion-sliding transition phase and the ring domain

$6 \leq r \leq 7$ and $\theta \cong 180$ ° as a strong adhesion domain corresponding to the critical range in the contact area where there is a risk of crack initiation under fretting.

Next, we do a field analysis of the principal stresses (Fig. 10).

The analysis of these graphs shows that the maximum principal stress σ_1 found between the edge of the hole and the edge of the contact area is maximum positive (σ_1 = 292 MPa) at r = 7.5 mm, $\theta \leq$ 179.81° and minimal (σ_1 = 282 MPa) at r = 2.5 mm or r = 12.5 mm, θ = 0 °, which confirms that this position is the most damaged position. This constraint is varied in the XY plane. The principal intermediate stress is constant (σ_2 = 0.75 MPa) whatever the angle and the radius in the XY plane, and the principal stress σ_3 is also varied in the XZ plane, it takes a minimum value at the edge of the hole (σ_3 = -2.19 MPa) and increases until reaching its maximum value.

According to these results, the position of crack initiation and propagation can be easily localized. The risk of crack initiation will happen in an inclined plane of an angle of θ = -90° with respect to the plane of application of the cyclic load at the edge of the hole: $P(r,\theta,z)$ = {r = 7.5 mm, θ = - 90, z = 1.6 mm} and P(r,θ,z) = {x = 0, y = - 7.5 mm, z = 1.6 mm}.

This results shows a good agreement between simulation and the experimentation according to the experimental work [31] (Fig. 1).

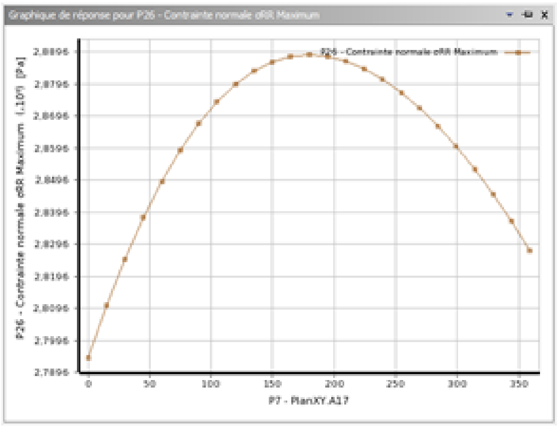

$\sigma_{rr} = f(r)$

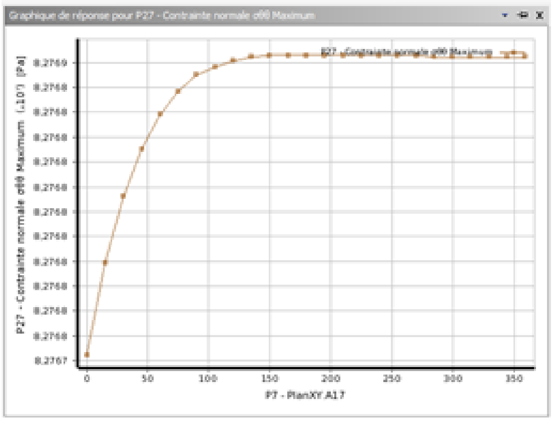

$\sigma_{\theta\theta} = f(r)$

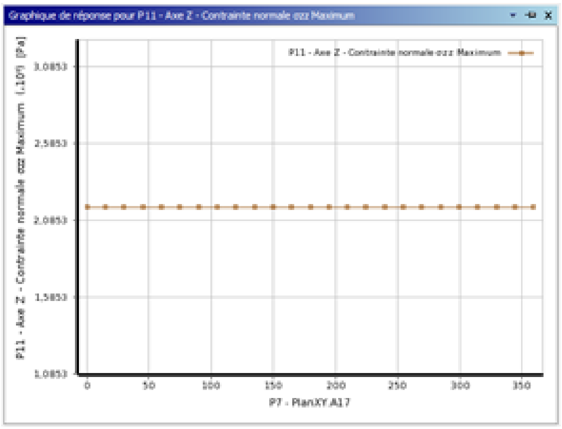

$\sigma_{zz} = f(r)$

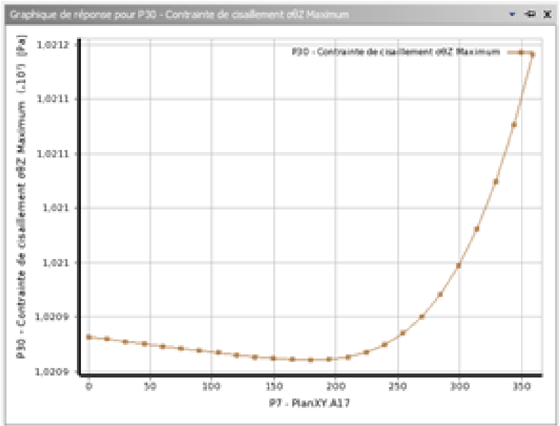

$\sigma_{\theta z} = f(r)$

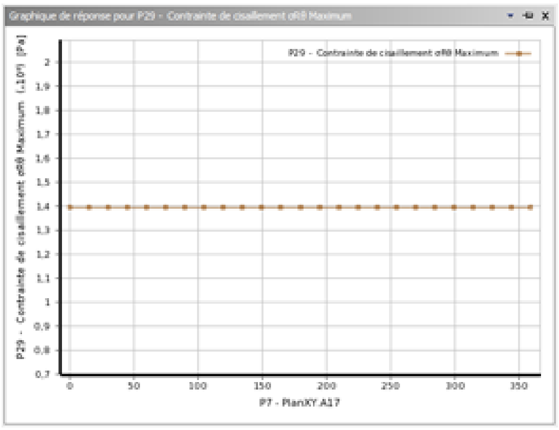

$\sigma_{r\theta} = f(r)$

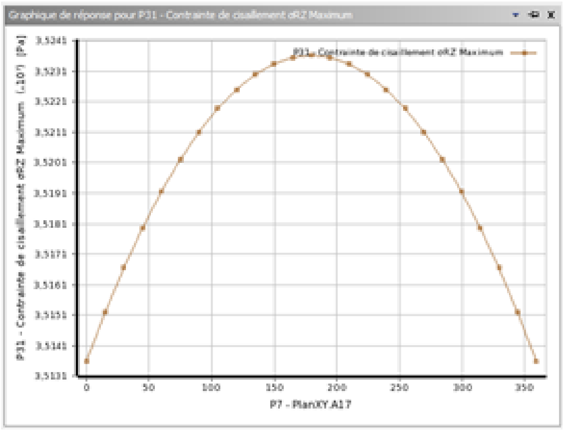

$\sigma_{rz} = f(r)$

Fig. 7. Distribution of stresses in cylindrical coordinate between the edge of the hole and the edge of the contact area.
(full colour version available online)

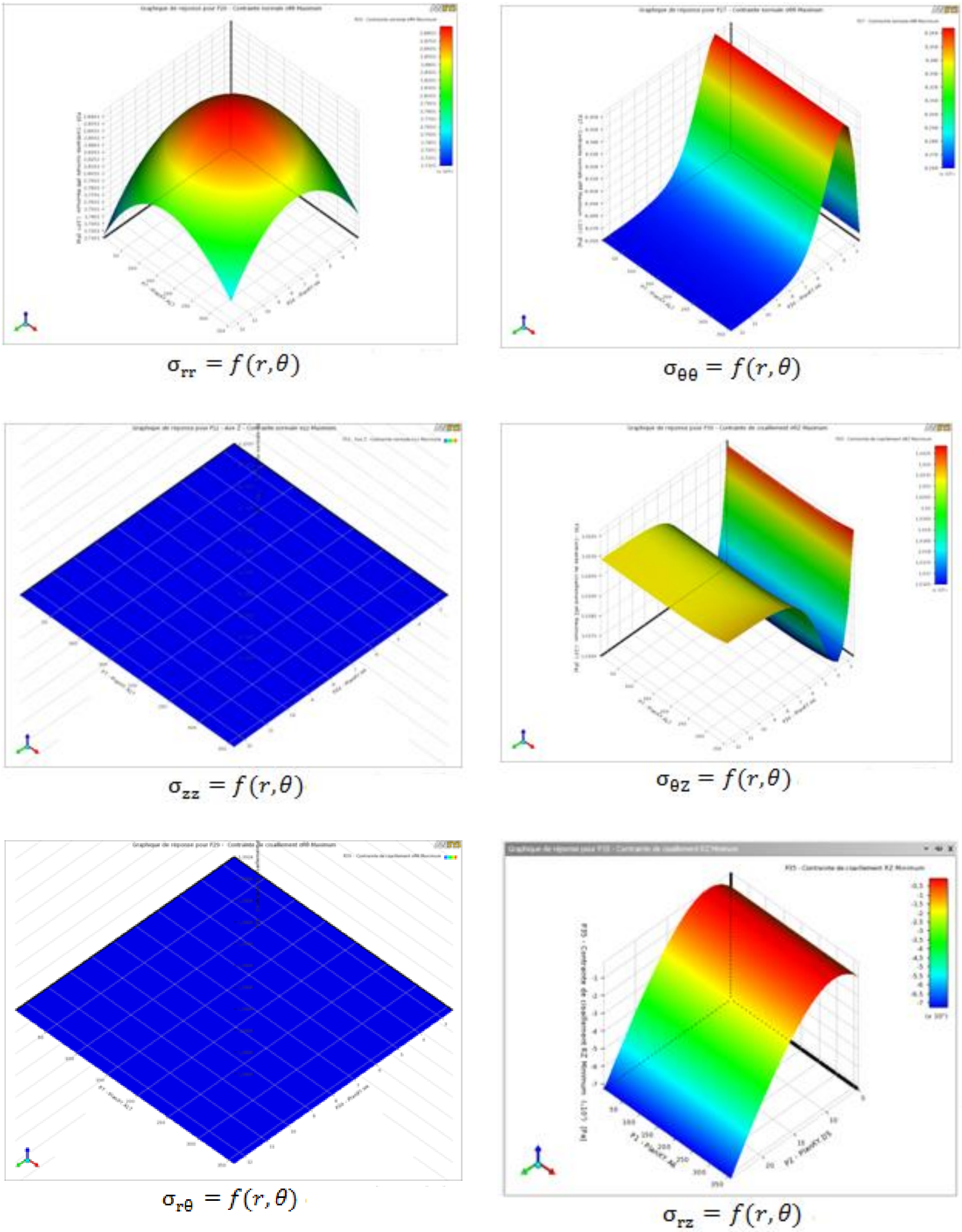

Fig. 8. Distribution of iso values of stresses in cylindrical coordinate between the edge of the hole and the edge of the contact area.
(full colour version available online)

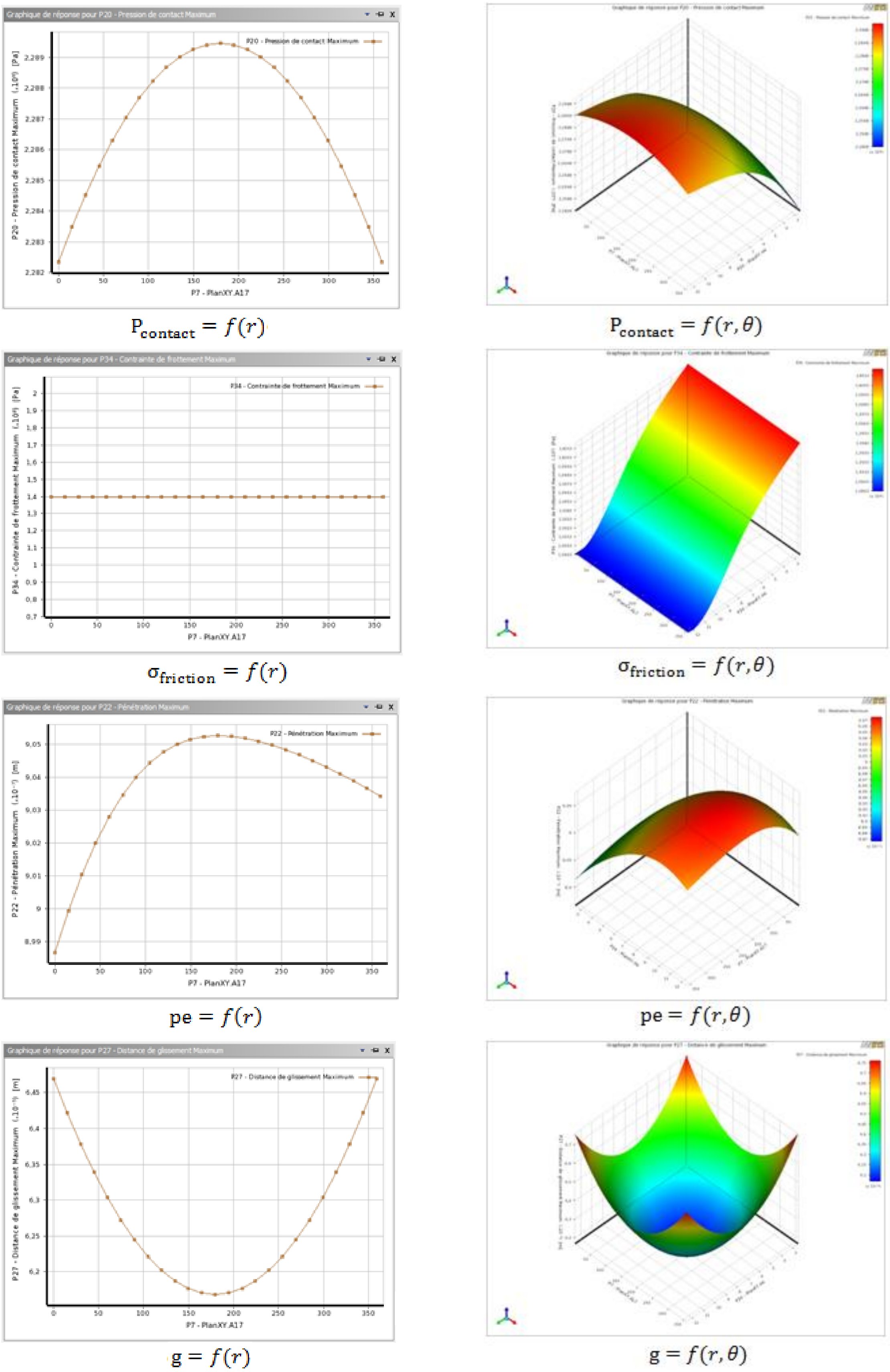

Fig. 9. Distribution of contact pressure, frictional stress, penetration and sliding between the edge of the hole and the edge of the contact area.
(full colour version available online)

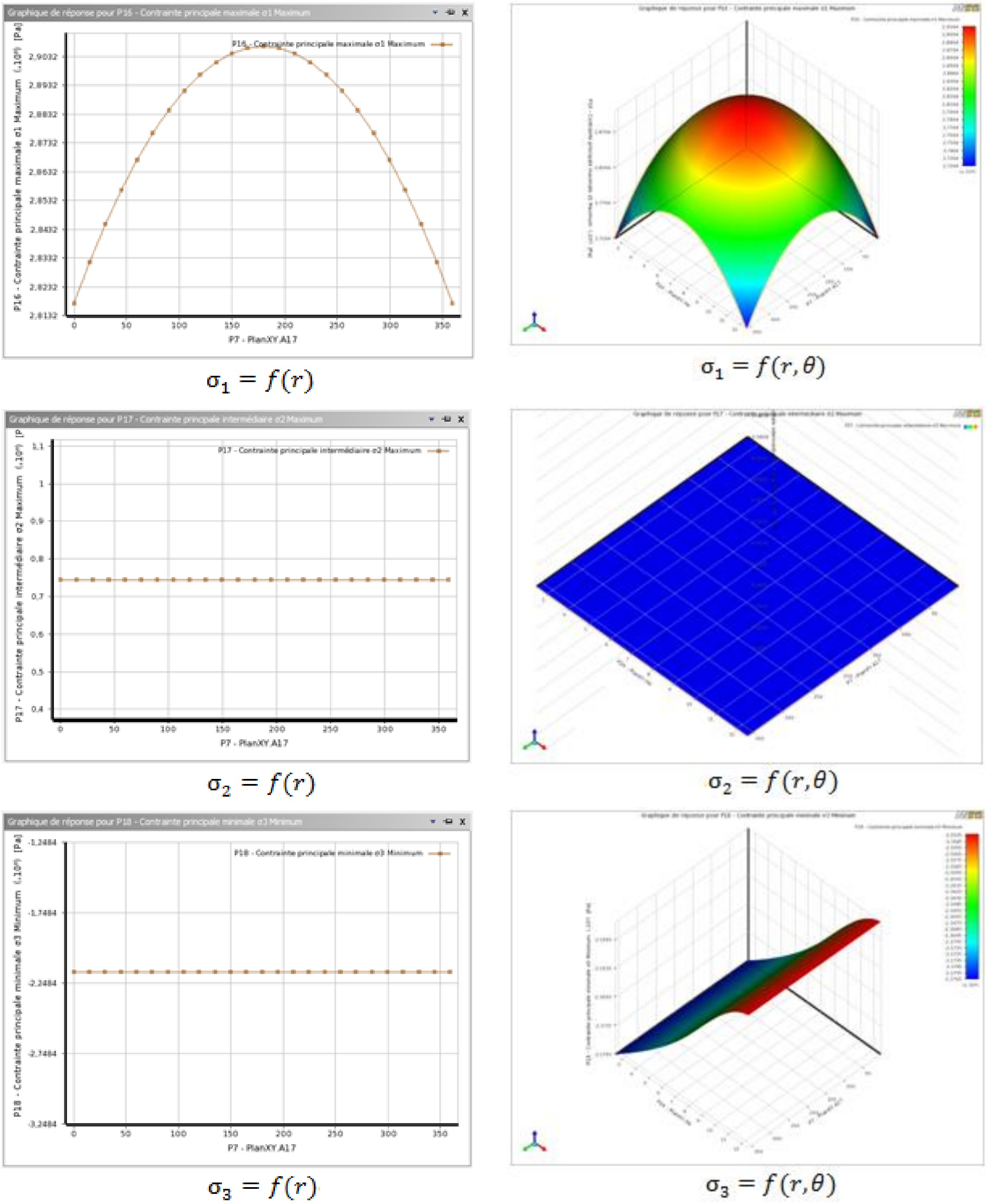

Fig. 10. Distribution of principal stresses between the edge of the hole and the edge of the contact surface.
(full colour version available online)

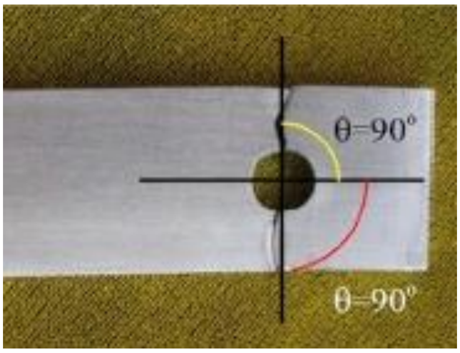

Fig. 11. Experimental rupture mode [31].

(full colour version available online)

5. Conclusion

The numerical simulation carried out in 3D, makes it possible to describe the real behaviour of a bolted assembly in fretting fatigue. The results obtained show that the tightening torque plays a significant role in the load transfer.

The distribution of the stress field is influenced by several parameters that can be summarized in the following:

– Technological parameters related to the design.

– Numerical parameters represented by the number of elements and the step of the computing time.

– The parts with strong stress concentrations of Von-Mises are generally found in the fasteners and the tracks of friction, causing mechanical phenomena (cracks, wear, rupture etc.…).

– The intensity of tightening torque involves the increase in the equivalent pressures of Von Mises, the shear stresses and the increase in the normal constraints in the plates.

– The constraints of Von-Mises of the plates increase in a notable way when the cyclic aspect charges and tightening torque are coupled.

– The place of crack initiation will be transferred to the edge of the zone of contact in a tilted plan from an angle equal to α = 90° compared to the direction from the slip.

References

[1] S. R. Lampman: ASM Handbook: Volume 19: Fatigue and Fracture, ASM International, 1997.

[2] E.M. Eden, W.N. Rose, F.L. Cunningham: Proc. I. Mech. Eng. 4 (1911) pp. 839-974.

[3] G. A. Tomlinson: Proceedings of the Royal Society of London 115A (1927) pp. 472–483.

[4] R.B. Waterhouse: Wear 100(1–3) (1984) 107-118.

[5] J.L. Mo, M.H. Zhu, J.F. Zheng, J. Luo, Z.R. Zhou: Tribol. Int. 43(5-6) (2010) 912–917.

[6] M.X. Shen, M.H. Zhu, Z.B. Cai, X.Y. Xie, K.C. Zuo: Tribol Int. 48 (2012) 162–171.

[7] D.-G. Kim, Y.-Z. Lee: Wear 250(1-2) (2001) 673-680.

[8] A.L. Mohd Tobi, J. Ding, S. Pearson, S.B. Leen, P.H. Shipway: Tribol. Int. 43(10) (2010) 1917-1932.

[9] D.K. Dwivedi, T.S. Arjun, P. Thakur, H. Vaidya, K. Singh: J. Mater. Proc. Tech. 152(3) (2004) 323-328.

[10] R.B. Waterhouse.: Fretting fatigue. Edité par Applied Science Publishers, UK, 1981

[11] A.J. Fenner, J.E. Field: Proc. N.E. Coast Institute of Engineers and Shipbuilders 76 (1960) 183.

[12] K. Nishioka, K. Hirakawa: Bulletin of the of the Japan Society of Mechanical Engineers 15 (1972) pp. 135-142.

[13] R. Bramhall: Studies in Fretting Fatigue, PhD thesis, University of Oxford, 1973.

[14] A. Mugadu, D.A., Hills, D. Nowell: Wear 252 (5-6) (2002) 475-483, 2002.

[15] C. Ruiz, P.H.B Boddington, K.C. Chen: Experimental Mechanics 24(3) (1984) 208-217.

[16] P. Papanikos, S.A. Meguid: Fatigue Fract. Eng.

Mats. Struct. 17 (1994) 539-550.

[17] B.P. Conner, T. Nicholas: ASME Jnl. Eng. Mats. Tech., in press, 2004.

[18] M. Friák, W.A. Counts, D.C. Ma, B. Sander, D. Holec, D. Raabe, J. Neugebauer: Materials 5 (2012) 1853-1872.

[19] H. Palkowski, S. Brück, T. Pirling, A. Carradò: Materials 6 (2013) 5118–5130.

[20] H.Y. Dong, W.L. Cao, J.H. Bian, J.W. Zhang: Materials 7 (2014) 7843–7860.

[21] S. Shkarayev, S. Mall: J. Strain Anal. Eng. Design 38 (2003) 495-506.

[22] S. Mall, V.K. Jain, H.A. Fadag: Strain 47 (2011) e305–e318.

[23] N. Moës, J. Dolbow, T. Belytschko: Int. J. Numer. Meth. Eng. 46 (1999) 131-150.

[24] B. Sonon, T.J. Massart: Materials 6 (2013) 5568–5592.

[25] D.S. Duglade: J. Mech. Phys. Solids 8 (1960) 100-104.

[26] G.I. Barenblatt: Adv. Appl. Mech. 7 (1962) 55–129.

[27] T.N. Chakherlou, M. Mirzajanzadeh, J. Vogwell: ENg. Fail. Anal. 7(16) (2009) 2066-2080.

[28] Military Handbook, Metallic Materials and Elements for Aerospace Vehicle Structures. USA, 1998.

[29] Swanson Analysis Systems Inc. ANSYS, User's guide for revision11, ANSYS 11 Documentation, ANSYS Element reference, Element, library. SOLID45/CONTA173.

[30] Groupe de Travail 11, Livre d'assemblages sous chargement statique, leçon 11.3.2 assemblages à boulons précontraints (Work group 11, Book of Assemblies under static loading, Pre-stressed bolt assemblies) (in French).

[31] A. Benhamena: Contribution à l'étude de l'endommagement en Fretting Fatigue des assemblages par fixation: Cas des Assemblages Rivetés (Contribution to the Fretting Fatigue Damage Study of assemblies by fixation: Rivet Assemblies Case). PhD Thesis, Sidi Bel Abbes, Algeria 2010 (in French).

DRY SLIDING WEAR BEHAVIOUR OF AUSTENITIC STAINLESS STEEL COATED WITH COBALT BASED ALLOY

Pushpinderjit Singh[1*], Amit Handa[2], Surendra Singh[3]

[1] Ludhiana College of Engineering and Technology, Katani Kalan, Ludhiana, Punjab, India.
[2] Department of Mechanical Engineering, IKG Punjab Technical University Campus, Hoshiarpur, Punjab, India.
[3] Indian Institute of Technology, Roorkee, Uttrakhand, India.
[*]corresponding author: e-mail: er.pushpinderjit@gmail.com

Resume

Surface coating techniques have a very important place in metal technologies. The aim of surface coating operations is to improve and enhance the properties of a material. In this study AISI 316L stainless steel was coated with cobalt base Stellite-6 alloy powder using Detonation Gun thermal spray process. After the coating deposition, the wear resistance of surface- alloyed layer was investigated using the pin on disc dry sliding wear test. The surface morphology of worn specimens was examined using scanning electron microscopy (SEM). The results obtained from all the tests were compared to those of bare AISI 316L specimens. For comparison of substrate and coated material, graphs were plotted. The wear resistance of coated specimens improved remarkably as compared to the bare specimens.

Available online: http://fstroj.uniza.sk/journal-mi/PDF/2017/06-2017.pdf

Article info

Article history:
Received 11 March 2017
Accepted 11 May 2017
Online 05 December 2017

Keywords:
Thermal spray coating;
AISI 316L;
Stellite-6 alloy;
Dry sliding wear;
Scanning Electron Microscopy (SEM).

ISSN 1335-0803 (print version)
ISSN 1338-6174 (online version)

1. Introduction

In a wide variety of applications, mechanical components have to operate under severe conditions, such as high load, speed or temperature and hostile chemical environment. Thus, their surface modification is necessary in order to protect them against various types of degradation. The thermal spraying has emerged as an important tool of increasingly sophisticated surface engineering technology. The different properties of the coating provide corrosion resistance, wear resistance, better thermal or electrical conductivity etc. [1]. AISI 316L, austenitic stainless steel is widely used in corrosive environments as it has high corrosion resistance. However, its wear, cavitation and erosion resistances are poor due to low hardness (220 HV), which restricts its use in many industrial applications [2]. Austenitic stainless steel exhibits a sticking behavior during the wear test, which is a distinctive feature of ductile materials that are capable of absorbing much larger quantities of energy before failure [3].

Coating a material with another material is done to obtain a combination of properties that combine the properties of the base material with other necessary properties that give corrosion resistance, wear resistance, better thermal or electrical conductivity [4].

The Stellite-6 is the most widely used cobalt based alloy exhibiting excellent resistance to many forms of mechanical and chemical degradation. Its applications include valve seats and gates, pump shafts, bearings and erosion shields. The exceptional wear resistance of Stellite-6 is mainly due to the unique and inherent characteristics of the hard carbide phase dispersed in the Co-Cr alloy matrix [5].

This paper deals with influence of the Stellite-6 coating on AISI 316L stainless steel. The specimens were subjected to pin-on-disc dry sliding wear test on a tribometer to investigate their wear resistance.

2. Experimental procedure

Stellite-6 alloy in powder form was used as coating material, the nominal composition of which is shown in Table 1.

The substrate material used was AISI 316L stainless steel, that is an extra low carbon version of 316 steel alloys. The low carbon content in AISI 316 L Stainless Steel prevents the formation of carbide on the surface when material comes in contact with heat. This can be used for bearings which operate in corrosive environments such as running inside liquids. However this steel has slightly lower mechanical properties. This steel fails mainly due to wear and elevated temperatures.

The chemical composition of substrate material is given in Table 2.

Before coating, the material was machined and specimens for dry sliding wear test were prepared.

2.1 Specimens for wear test

For dry sliding wear test, specimens of diameter 10 mm x 30 mm length were prepared by cylindrical turning on the lathe. Both sides of the specimens were ground on a surface grinder.

Table 1

The chemical composition of Stellite-6.

Element	**Cr**	**W**	**C**	**Ni**	**Fe**	**Si**	**Mn**	**Mo**	**Co**
Wt. %	28.60	4.90	1.30	0.65	0.79	1.25	1.13	<0.10	Bal.

Table 2

Chemical composition of AISI 316 L.

Element	**C**	**Si**	**Mn**	**P**	**S**	**Ni**	**Cr**	**Mo**	**Fe**
Wt. %	0.020	0.400	1.320	0.026	0.030	10.270	16.570	2.010	Bal.

Table 3

Technical Specification of Awaaz Detonation Gun.

Working Gases	Oxygen, Acetylene, Nitrogen and Air
Consumption of Powder per Shot	0.02-0.05g/ shot
Water Consumption Rate	15-25 litres/minute
Firing Rate	1-10 Hz
Coating Thickness per Shot	5-25 μm
System Control	Manual/ Semi auto
Dimensions (L X B x H) mm	1200 x 500 x 1500
Sound Pressure Level	150 dB

Table 4

Process parameters for Stellite-6 coating by D- gun thermal spray process.

Parameter	Value
Oxygen Flow Rate	52 SLPM (Standard Litres Per Minute)
Pressure	0.2 MPa
Acetylene Flow Rate	40 SLPM (Standard Litres Per Minute)
Pressure	0.14 MPa
Nitrogen Flow Rate	17.33 SLPM (Standard Litres Per Minute)
Pressure	0.4 MPa
Spray Angle	90˚
Spray Distance	150 mm
Power	450 VA

2.2 Coating of specimens

For coating process the equipment used was "Awaaz Detonation Gun" available at M/s SVX Powder M Surface Engineering Pvt. Ltd., Greater Noida (India). The technical specifications of the detonation gun are given in Table 3. The process parameters for thermal spray Stellite-6 coating by detonation gun are given in Table 4. The specimens to be coated were firstly sand blasted using alumina powder (Al_2O_3) to make the surface rough and suitable for coating deposition.

2.3 Testing of specimens

Pin on Disc Wear Test: The dry sliding pin on disc wear test was carried out on the Wear and Friction Monitor TR- 20, make M/s Ducom Bangalore, India. The machine is equipped with digital display for friction, time and rpm. It has got a variable speed motor so that speed can be set for the test. The tribometer is shown in Fig. 1.

Fig. 1. Pin on Disc wear tester (Ducom TR-20).
(full colour version available online)

The specimens (pins) were weighed before and after the wear test to determine the weight loss. The specimens were weighed on 0.0001 gm precision balance. The test was performed using ASTM G99 standard. The D2 die steel was used to prepare the disc used as counterface. The plate was hardened to a hardness value of HRC 62-65 and ground on a surface grinder. The loading conditions were varied from lighter to severe, as shown in Table 5, whereas Track diameter, speed of disc and time of test were kept constant. The various parameters of dry sliding wear test are shown in Table 5.

Scanning Electron Microscopy: After the dry sliding pin on wear test, the surface morphology of worn specimens was observed at Sophisticated Analytical Laboratories, Thapar University, Patiala. The equipment used was JEOL JSM-6510 LV Scanning Electron Microscope, which is a low vacuum scanning electron microscope. This machine has got a magnification range of 5× to 300,000×. The accelerating voltage of the machine is from 0.5 to 30 kV. The machine can enable the observations of specimens up to 150 mm in diameter. The JEOL JSM-6510 scanning electron microscope is depicted in Fig. 2.

Fig. 2. JSM-6510 LV Scanning Electron Microscope.
(full colour version available online)

Table 5

Parameters for Dry Sliding Wear Test.

Applied Normal Load (N)	19.6, 29.4 and 49 (varied over three levels)
Speed of Disc (r.p.m.)	500 (kept constant)
Track diameter	80 (kept constant)
Time (minutes)	5 (kept constant)

3. RESULTS AND DISCUSSION

3.1 Dry Sliding Wear Test

The pin on disc dry sliding wear test was performed on the bare and coated specimens. The track diameter was kept constant at 80 mm and the rotational speed of disc was kept constant at 500 rpm, with load varying as 19.6, 29.4 and 49 N. The disc was prepared of the D2 die steel with a hardness of 62 HRC. The wear rate of the specimens was calculated using the previously mentioned formula.

$$W_s = \frac{\Delta m}{\rho L F} \times 10^{-12} \quad (1)$$

where W_s is the wear rate in $mm^3 \cdot Nm^{-1}$, Δm is the mass loss of test specimens during the wear test at N revolutions, in gm, ρ is the density of test materials in $gm \cdot cm^{-3}$, L is the total sliding distance in m and F is the normal force acting on the pin in N. The sliding distance is obtained as a product of the linear velocity and time, while the linear velocity is equal to,

$$V = \frac{2\pi R N}{60} \quad (2)$$

where R is track radius and N is disc speed in rpm.

The wear rate of the uncoated specimens was found to increase with increment of the normal load. This is due to low hardness of the bare AISI 316L specimens. The weight loss of the uncoated specimens increased for all the specimens. The wear rate of Stellite-6 coated specimens decreased with increase of the normal load. This is due to the high hardness of the coated specimens and wear resistant properties of the Stellite-6. The test results of the dry sliding wear test are represented graphically in Fig. 3.

3.2 Morphology of worn surfaces

The specimens tested on the pin on disc tribometer were examined on a scanning electron microscope (SEM) to evaluate the surface characteristics of the uncoated and the Stellite-6 coated specimens.

Morphology of worn surface of the uncoated AISI 316L specimens: The scanning electron micrographs of worn surfaces for the uncoated specimens are shown in Figs. 4 to 6. The micrographs support the results of the mass loss obtained during the dry sliding wear test. Fig. 4 shows the SEM images of wear tracks after the dry sliding wear test of the uncoated AISI 316L specimen at 19.6 N load. The material removal from the wear track was caused by adhesive and abrasive wear. The wear is less severe and the less number of debris are formed. The plastic deformation is limited and the linear wear tracks are visible.

The SEM image of the worn surface of the uncoated AISI 316L specimen at 29.4 N load is shown in Fig. 5. The micrograph supports the fact that the wear is more severe in this case due to increased load. Numerous debris in shape of small balls can be clearly seen in the SEM image. The abrasive wear caused during the test also is shown by the grooves created in the wear tracks. This is due to the effect of micro-ploughing. In addition to this, fins are also observed on the edges of the wear tracks. These will eventually break off, resulting in higher mass loss.

Fig. 6 shows the SEM image of the worn surface of the uncoated AISI 316L specimen at 49 N load. The phenomenon of delamination is observed. The material from the worn surface is pulled out from the specimen and voids are created. The friction also plays an important role in this observation, since due to rise of temperature the material tends to deform plastically and hence voids and gaps are created. The fins created during the sliding wear are now much more clearly visible on the edges of tracks, which tend to overlap each other due to the temperature rise and plastic deformation of the uncoated bare AISI 316L specimen.

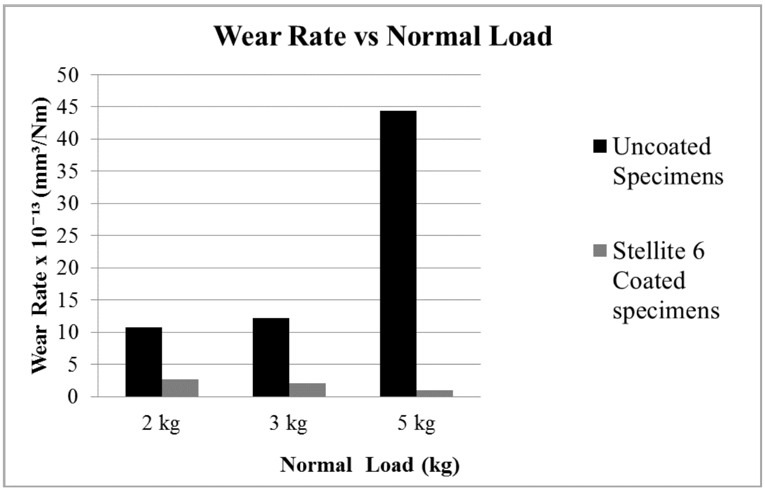

Fig. 3. Graphical representation of Dry sliding pin on disc wear test.

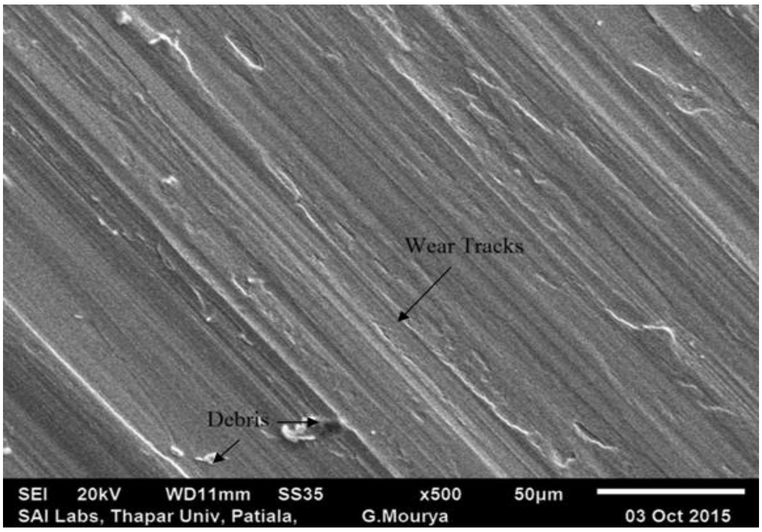

Fig. 4. The SEM image of worn surface of the uncoated AISI 316L specimen at 19.6 N, 2.09 m·s^{-1} speed.

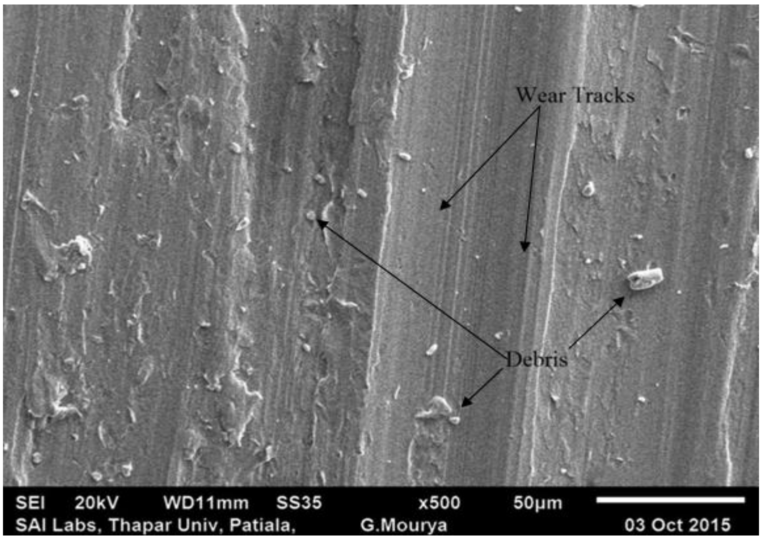

Fig. 5. The SEM image of the worn surface of the uncoated AISI 316L specimen at 29.4 N, 2.09 m·s^{-1} speed.

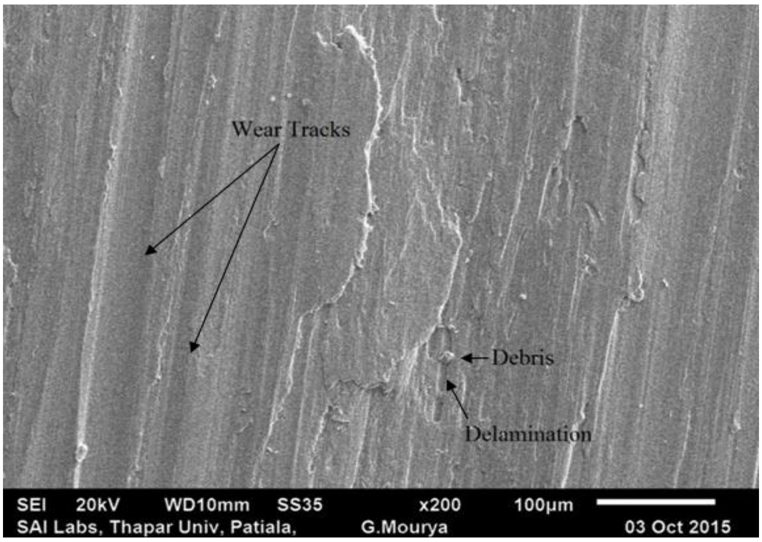

Fig. 6. The SEM image of the worn surface of the uncoated AISI 316L specimen at 49 N, 2.09 m·s^{-1} speed.

Morphology of the worn surface of the Stellite-6 coated AISI 316L specimens: The scanning electron micrographs of the worn surfaces for the Stellite-6 coated AISI 316L specimens are shown in Figs. 7 to 9. Fig. 7 shows the behaviour of the Stellite-6 coated AISI 316L steel specimens after the dry sliding wear test at 19.6 N load. The wear tracks are smooth in general and partially damaged regions are observed. There is no severe damage or grooving as compared to that of the uncoated AISI 316L specimens.

Fig. 8 shows the behaviour of the Stellite-6 coated AISI 316L steel specimens after the dry sliding wear test at 29.4 N load. It is observed that wear tracks are not continuous. This behaviour is in support of the mass loss results of the dry sliding wear test. The mass loss of the Stellite-6 coated specimens was less as compared to the uncoated AISI 316L specimens. Some debris is also observed on the wear tracks, but there is no grooving or delamination.

Fig. 9 shows the behaviour of the Stellite-6 coated AISI 316L steel specimens after the dry sliding wear test at 49 N load. The wear tracks are very smooth and fine lines are observed on the worn surface. This is due to the temperature rise at high loading conditions caused by friction. The debris formed is also attached to the surface and does not fall off the surface. This is the reason of the less mass loss. The wear of the surface is superficial and no major damage is observed.

4. CONCLUSIONS

In the light of the results obtained during the course of present investigation, it is inferred that:

- The wear rate of the Stellite-6 coated specimens was much less as compared to the uncoated AISI 316L steel specimens. Thus, it may be concluded that as the loading conditions get severe, the behaviour of the Stellite-6 coated specimens improved whereas for the uncoated specimens, the wear behaviour decreased with further increase of normal load. Therefore, it is inferred that the Stellite-6 coated AISI 316L specimens are better suited for more severe conditions of the dry sliding wear.
- The wear signs on the bare specimens were deep and clear due to micro-ploughing and grooving. However, the wear signs on the Stellite-6 coated specimens were more superficial.

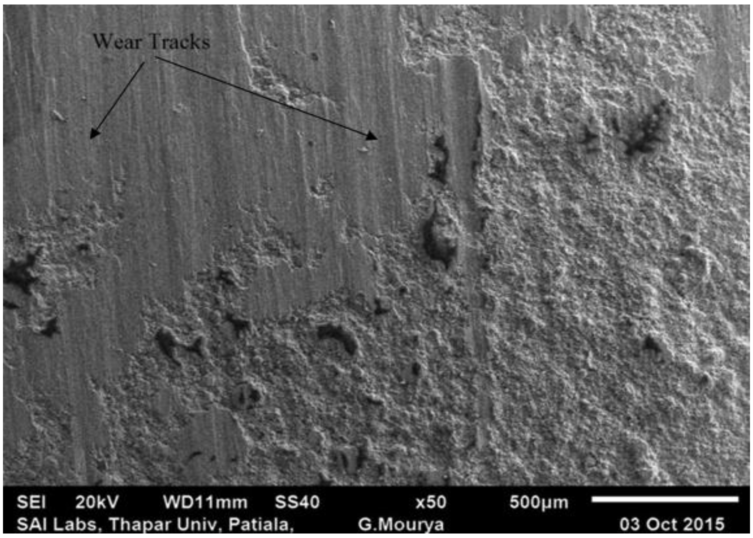

Fig. 7. The SEM image of the worn surface of the Stellite-6 coated AISI 316L specimen at 19.6 N, 2.09 m·s^{-1} speed.

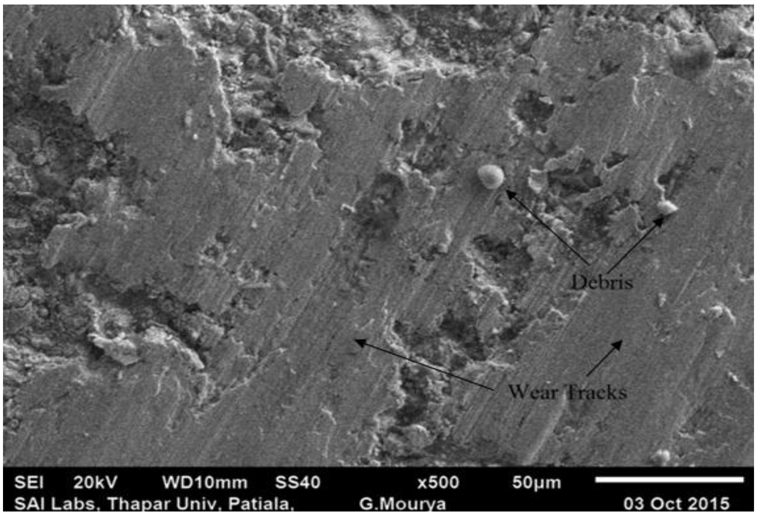

Fig. 8. The SEM image of the worn surface of the Stellite-6 coated AISI 316L at 29.4 N, 2.09 m·s^{-1} speed.

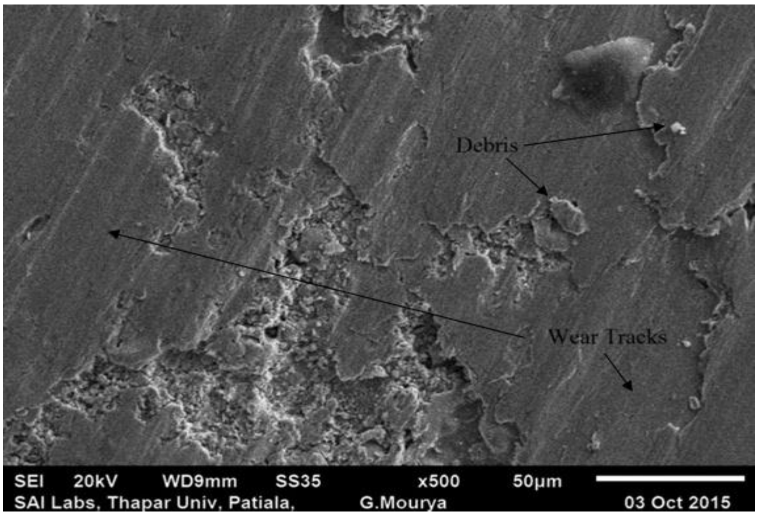

Fig. 9. The SEM image of the worn surface of Stellite-6 coated AISI 316L specimen at 49 N, 2.09 m·s^{-1} speed.

References

[1] B.S. Sidhu, D. Puri, S. Prakash: J. Mater. Proces. Tech. 159 (2005) 347-355.

[2] A. Viswanathan, D. Sastikumar, H. Kumar, A.K. Nath: J. Mater. Process. Technol. 203 (2009) 1618-1623.

[3] A. Dalmau, W. Rmili, D. Joly, C. Richard, A. Igual-Munoz: Tribol. Lett. 56 (2014) 517-529.

[4] F. Molleda, J. Mora, F.J. Molleda, E. Mora, E. Carrillo, B.G. Mellor: Mater. Charact. 57 (2006) 227-231.

[5] K. Prasad Rao, R. Damodaram, H. Khalid Rafi, G.D. Janaki Ram, G. Madhusudhan Reddy, R. Nagalakshmi: Mater. Charact. 70 (2012) 111-116.

[6] A.S.C.M. D'Oliveira, P.S.C.P. Da Silva, R.M.C. Vilar: Surf. Coat. Tech. 153 (2002) 203-209.

[7] S. Apay, B. Gulenc: Materials and Design 55 (2014) 1-8.

[8] P. Ganesh, A. Moitra, T. Pragya, S. Sathyanarayanan, K. Harish, S.K. Rai, K. Rakesh, C.P. Paul, R.C. Prasad, L.M. Kukreja: Mater. Sci. Eng. A 527 (2010) 3748-3756.

[9] Y. Zou, C.-Y. Zhan, B. Yang, J.-C. Wu: J. Nucl. Mater. 436 (2013) 56-60.

[10] M. Taguchi, H. Sumitomo, R. Ishibashi, Y. Aono: Mater. Trans. 49 (2008) 1303-1310.

[11] M.G. Hebsur, J.J. Moore: Eng. Fract. Mech. 22 (1985) 93-100.

[12] G. Xu, M. Kutsuna, Z. Liu, K. Yamada: Surf. Coat. Tech. 201 (2006) 1138-1144.

[13] A. Gholipour, M. Shamanian, F. Ashrafizade: J. Alloy. Compd. 509 (2011) 4905-4909.

[14] Q. Jing, Y. Tan: Mater. Res. 16 (2013) 1071-1076.

[15] O.P. Modi, B.K. Prasad, A.K. Jha, V.P. Deshmukh, A.K. Shah: Tribol. Lett. 17 (2004) 129-138.

[16] J.C. Shin, J.M. Doh, J.K. Yoon, D.Y. Lee, J.S. Kim: Surf. Coat. Tech. 166 (2003) 117-126.

[17] A. Tiziani, L. Giordano, P. Matteazzi, B. Badan: Mater. Sci. Eng. 88 (1987) 171-175.

[18] D. Uzunsoy: Materials and Design 31 (2010) 3896-3900.

[19] ASTM G99, "Standard Test Method for Wear Testing with a Pin- on- Disk Apparatus."

ON THE RECRYSTALLIZATION AND TEXTURE OF FE-36%NI ALLOY AFTER ACCUMULATIVE ROLL BONDING AND ANNEALING AT 600 °C

Kamel Tirsatine[1,*], Hiba Azzeddine[1,2], Thierry Baudin[3], Anne-Laure Helbert[3], François Brisset[3], Djamel Bradai[1]

[1] Faculté de Physique, Université des Sciences et de la Technologie Houari Boumediene, Bab Ezzouar, BP32, El Alia, Alger, Algérie.
[2] Département de physique, Faculté des sciences, Université Mohamed Boudiaf, M'Sila, Algérie.
[3] ICMMO, Université Paris-Sud, Université Paris-Saclay, UMR CNRS 8182, 91405 Orsay Cedex, France.
[*]corresponding author: e-mail: ktirsatine7@yahoo.fr

Resume

Microstructure and texture evolution of Fe-36%Ni (wt. %) alloy after 1, 5 and 10 accumulative roll-bonding (ARB) cycles and annealing at 600 °C up to 3600 seconds were studied using electron backscatter diffraction. Microstructural and textural changes after ARB and annealing were compared to those existing in the literature after conventional rolling. The microstructure was not stable at 600 °C for all ARB samples even after 3600 seconds of annealing. The recrystallization texture was dominated by the Cube {001}<100> texture component. Recrystallization kinetics were determined using microhardness measurement and were close to those after cold rolling with Avrami time exponent around unity. The texture evolution at high strain was discussed in terms of grain boundary migration obstruction by the formation of layer interfaces and small recrystallized grains near the bonded interfaces.

Available online: http://fstroj.uniza.sk/journal-mi/PDF/2017/07-2017.pdf

Article info

Article history:
Received 24 October 2016
Accepted 19 June 2017
Online 05 December 2017

Keywords:
Invar;
Accumulative roll bonding;
Recrystallization kinetics;
Ultrafine grains;
Texture;
Microstructure.

ISSN 1335-0803 (print version)
ISSN 1338-6174 (online version)

1. Introduction

Thermo-mechanical processing of alloys is of great importance for industrial specific needs. The recrystallization microstructure, texture, nature and geometry of grain boundaries are key factors influencing the mechanical properties of materials. The understanding of recrystallization kinetics and texture evolution during severe plastic deformation, especially Accumulative Roll Bonding (ARB), allows the possibility to ensure optimal conditions during thermo-mechanical processing of alloys.

Ultrafine-grained metals or alloys have demonstrated a higher combination of strength and ductility than the coarse-grained ones [1]. After ARB processing, Fe-36%Ni (wt. %) alloy samples were strengthened up to 200 % relatively to the non-deformed initial state and exhibited an ultrafine microstructure with grains having elongated shape in the rolling direction [2, 3].

Despite the numerous papers dealing with microstructure and texture evolution analysis of Fe-36%Ni alloy after conventional rolling and recrystallization annealing [4 – 8], there is a lack of knowledge on the thermal stability of the ultrafine grained Fe-36%Ni (wt.%) alloy severely deformed by ARB. In this paper we present the detailed results of electron backscatter diffraction (EBSD) measurement on the evolution of the microstructure texture as well as recrystallization kinetics of the Fe-36%Ni (wt. %) alloy processed by ARB and annealed at 600 °C.

2. Experimental procedure

The fully recrystallized Fe-36%Ni (wt. %) alloy was kindly provided by APERAM alloys society, France. The ARB processing was carried out at 550 °C to 1, 5 and 10 cycles. The results of deformation texture and microstructure of the as deformed state were published by Tirsatine et al. [2]. Sheets of 1 mm thickness were cut from the ARBed samples and subsequently isothermally annealed at 600°C for 120, 600, and 3600 sec under H2 flux protection. The annealing temperature was selected by taking into account the results of [5].

Microstructure and microtexture was characterized using a FEG-SEM SUPRA 55 VP scanning electron microscope operating at 20 kV with the TSL Orientation Imaging Microscopy, OIMTM software. The samples were mechanically polished and then electro-polished for EBSD measurements. EBSD maps were recorded on 100 × 100 μm zones on the RD–ND (rolling and normal directions) plane of the annealed samples with a step size of 0.1 mm. The grain size data were obtained using a grain tolerance angle of 5° and the minimum grain size was chosen to be 2 pixels.

Quantitative texture analysis was carried out by calculating the Orientation Distribution Function (ODF) using the "Harmonic Method" implemented in the MTex software [9].

The micro-hardness of the specimens was measured with a Vickers microhardness tester SHIMADZU type HMV-2 using a load of 0.05 kg (HV0.05). Five hardness indentations were performed in the central area of the samples.

3. Results and discussion

3.1 Microstructure evolution after annealing of ARBed Fe-36%Ni alloy

Fig. 1 shows the orientation imaging micrographs (OIM) of Fe-36%Ni (wt. %) alloy samples after ARB processing to 1, 5 and 10 cycles and annealing at 600 °C for 120, 600 and 3600 sec. As reported earlier [2], the severely deformed microstructure of Fe-36%Ni (wt. %) alloy was characterized by elongated ultrafine grains. The grains underwent a strong refinement (down to 0.5 and 0.2 μm for length along RD and thickness along ND respectively) after 10 ARB cycles [2]. As can be seen from Fig. 1, a substantial evolution of the microstructure is noticed during annealing. The OIM of 1 ARB sample show a color gradients inside some grains which indicates that the recrystallization is not complete after annealing for 3600 sec. Contrarily, the evolution of the microstructure for 5 and 10 ARB samples looks similar and is associated to the apparition of massive and progressive recrystallization and subsequent grain growth.

Fig. 1 shows that the microstructural change during the annealing is similar to that reported in ARBed pure Cu that was associated with a typical discontinuous recrystallization mechanism [10] (Figs. 1e and f). Indeed, annealing process of pure Cu that is known to have a low stacking fault energy is different from that of materials with high stacking fault energy that are categorized as "recovery-type" [10]. Zaefferer et al. [5] reported that, Fe-36%Ni (wt. %) alloy has a relative stacking fault energy in between those of Cu and Al γrela(Cu):γrela(FeNi):γrela(Al)=1:3:7, γrela=γ/Gb (γ, stacking fault energy; G, shear modulus and b length of the Burgers vector). The authors showed a deformation and recrystallization texture behavior similar to that of pure Cu. Moreover, this alloy recovers very little during cold rolling (dynamic recovery) owing to its high melting temperature and high concentration of Ni.

In the peculiar zones shown by inserts in Figs. 1j-l, a spread of small grains all over the bonded interface between layers is clearly seen. The black colored areas (non-indexed points) in the inserts of Figs. 1j, k and l correspond to holes at the mid-thickness interface obtained after the last ARB cycle (Figs. 1a, d and g).

The presence of clustered small grains

near the bonding can be associated with the shear strain induced at the sheet surfaces, in contact with the rolls, at the cycle before the last one or can be due to the wire-brushing. In both cases, this strain induces a strong germination rate that results in a so small grain size. Takata et al. [10] have already mentioned that the presence of fine grains in the bonded interface was due to the redundant shear deformation or/and wire-brushing. In our case, we used a lubricated ARB process that probably limited shear strain, and it can be supposed that the fine grains, in the bonding area, are mainly due to the wire-brushing.

After 10 ARB cycles, the strip thickness is around 0.97 μm. The mean grain size measured by the line-intercept method is around 10 μm. This result shows clearly that a good bonding is achieved and the grains can cross the layer boundaries and grow all over the layer thickness. In fact, whatever the cycle number, the low bonding quality of the mid-thickness interface inhibits the boundary migration and thus the grain growth.

Fig. 2 shows the evolution of the grain diameter of all grains as well as the recrystallized grains of Fe-36%Ni alloy after ARB processing and annealing at 600 °C up to 3600 sec. The grain size was estimated from the equivalent circle diameter. Concerning the global grain size (all grains), it is clear that the grain diameter increases significantly upon annealing after 5 and 10 ARB cycles especially after 600 sec whereas it remains quite constant after 1 ARB cycle. In this alloy, the recrystallization mechanism corresponds to a discontinuous recrystallization as it can be observed in Fig. 1. This recrystallization consists in nucleation followed by nuclei growth into the deformed matrix by Strain Induced Boundary Migration (SIBM) mechanism [10] and it leads to equiaxed grains. In the special case of 1 ARB cycle, the appearance of recrystallized grains is delayed (Fig. 1g) because of the lower energy stored during the deformation processing. The grain size of 1 ARB sample remains constant because the recrystallized grains have the same equivalent diameter than the all grains at this special recrystallization time (Fig. 2, dotted lines). In the case of 5 and 10 ARB cycles, the grain size notably increases after annealing for 600 sec. Note that after 1 ARB cycle, the microstructure is partially recrystallized after 3600 sec annealing. On the contrary, for the same annealing time, the recrystallization is complete for the two largest cycle numbers. It has already been observed in the literature that the growth rate of the grains in the fine-grained material (like in 5 and 10 ARB samples) is some times faster than that of the coarse-grained material (like in 1 ARB sample) at the same temperature. Such difference in the recrystallization kinetics could be ascribed to the stored energy during the deformation [11]. Moreover, the achieved grain diameter after annealing for 360 sec is close to the initial grain size of the unprocessed material ($8 < d < 10$ μm) [2]. Unfortunately, this ARB processing route does not maintain a refined microstructure after complete recrystallization, contrary to the ECAE processing of a Copper alloy (3 μm) [12].

Furthermore, it can be observed that the achieved grain size is slightly more important after 5 ARB cycles (11 μm) than after 10 ARB cycles (8 μm). This can be explained by the fact that after 10 ARB cycles the deformation amount is larger, thus the nucleus number is increased and, as a consequence, the final grain size is smaller.

Fig. 3 shows the evolution of the twin fraction as a function of ARB cycle number and annealing time. The increase of twin fraction is consistent with the occurrence of the discontinuous recrystallization and the associated grain growth [13]. Additionally, it is seen that twin fraction after complete recrystallization is similar (around 40 %) whatever the ARB cycle number 5 or 10.

Fig. 4 presents the evolution of high angle grain boundary (HAGB) fraction of the Fe-36%Ni (wt. %) alloy after ARB processing and annealing at 600 °C for 120, 600 and 3600 sec. The evolution of HAGB fraction shows an increase after 1600 sec as recrystallization develops. The HAGB fraction reaches 80 % after complete recrystallization for 5 and 10 ARB samples (annealing for 3600 sec), which indicates that the alloy is not isotropic (HAGB > 95 %). The low HAGB fraction (about 40 %) for 1 ARB sample is due to the partial recrystallization of the sample.

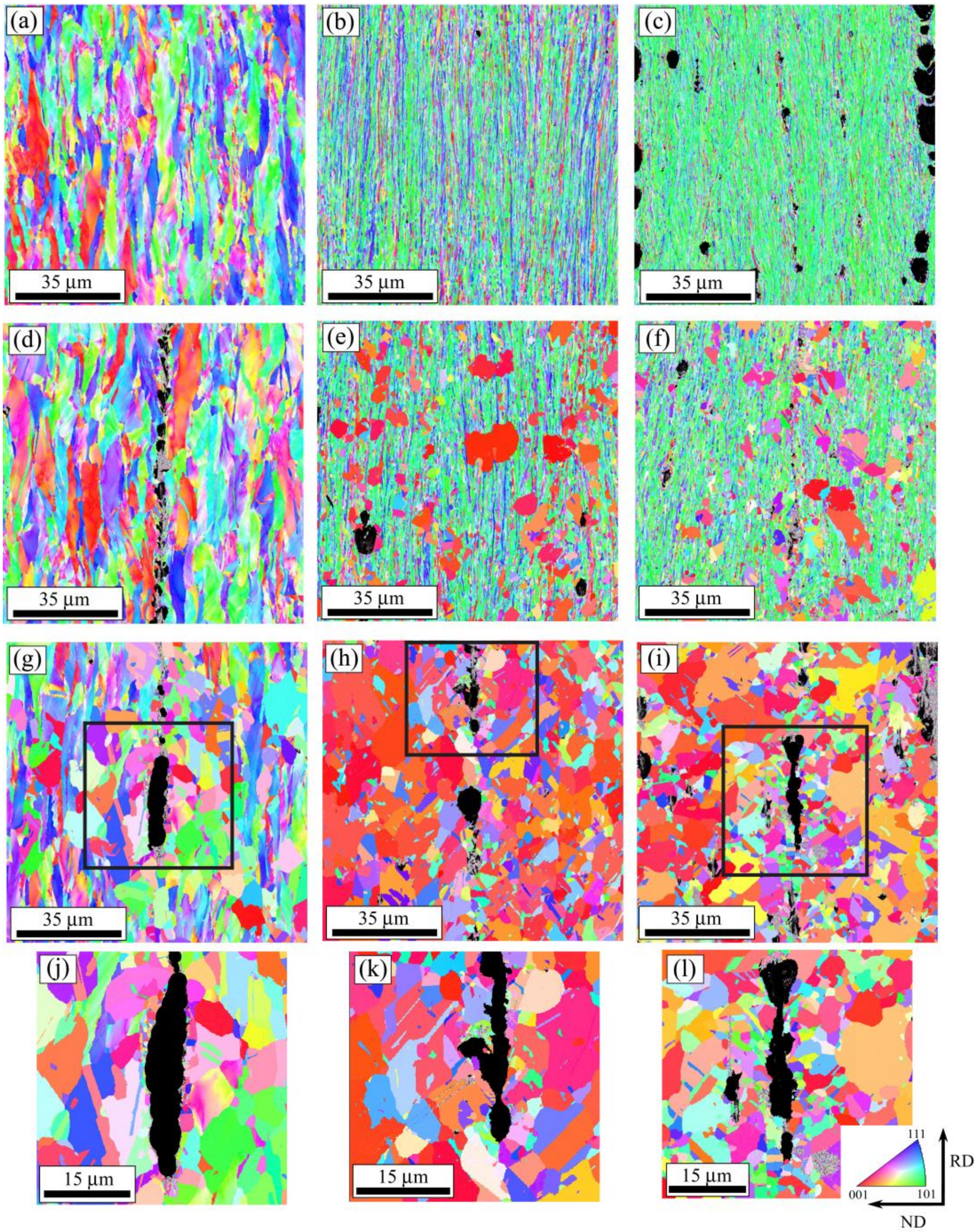

Fig. 1. OIM of Fe-36%Ni (wt. %) alloy after ARB processing to 1cycle and annealed at 600° C for (a) 120 sec, (b) 600 sec, (c) 3600 sec, 5 cycles and annealed at 600 °C for (d) 120 sec, (e) 600 sec, (f) 3600 sec and 10 cycles and annealed at 600 °C for (g) 120 sec, (h) 600 sec, (i) 3600 sec. Peculiar zones near bonding zones are shown as inserts.

(full colour version available online)

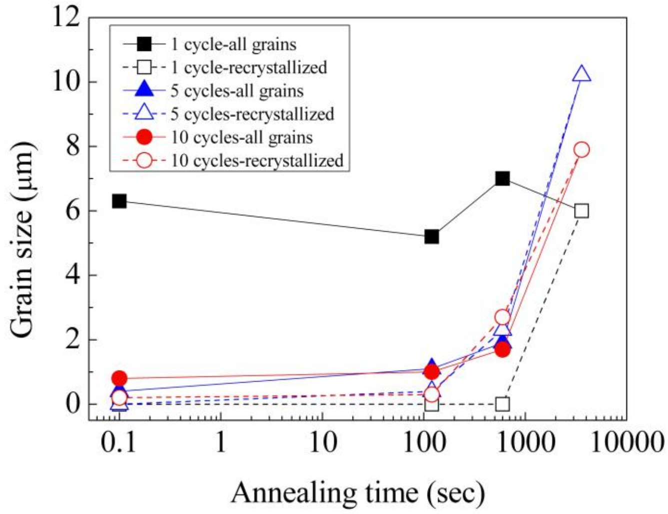

Fig. 2. Evolution of the grain diameter of all grains and the recrystallized grains of Fe-36%Ni (wt. %) alloy after ARB processing and annealing at 600 °C up to 3600 sec.
(full colour version available online)

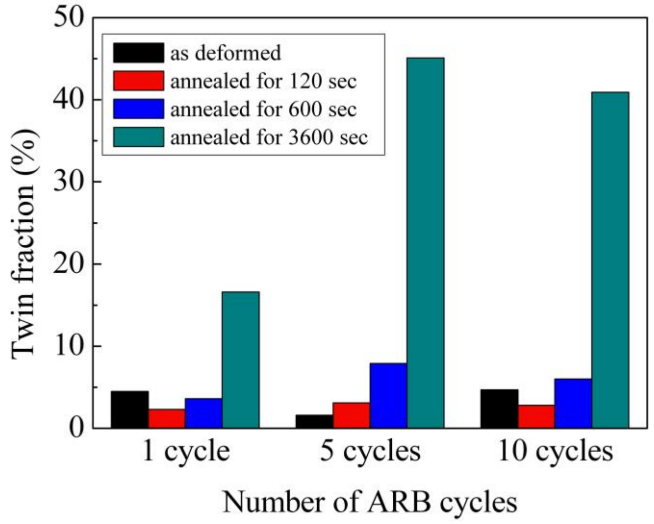

Fig. 3. Evolution of the Twin fraction as a function of ARB cycle number and annealing time.
(full colour version available online)

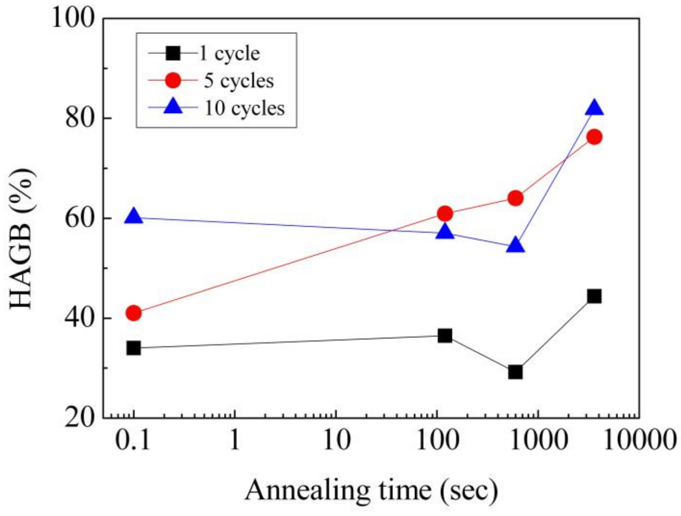

Fig. 4. Evolution of HAGB fraction of Fe-36%Ni (wt. %) alloy after ARB processing and annealing at 600 °C up to 3600 sec.
(full colour version available online)

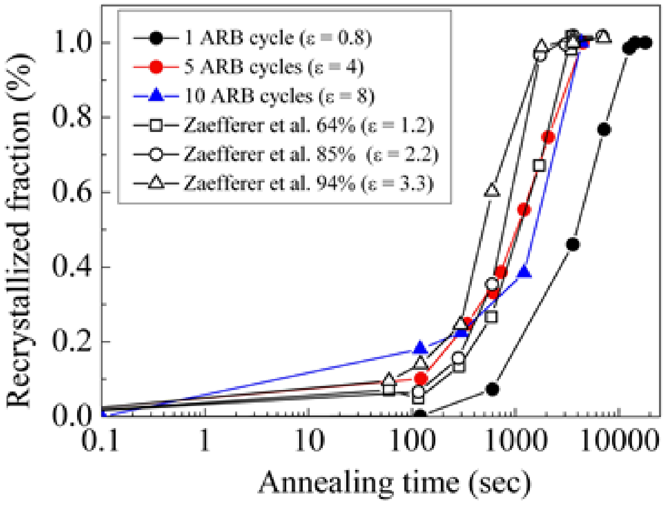

Fig.5 Recrystallized volume fraction versus annealing time of the Fe-36%Ni (wt. %) alloy after ARB processing and annealing at 600 °C. Data from Reference [5] are shown for comparison.
(full colour version available online)

Table 1
The JMAK parameters variation determined in the present study. Results from Zaefferer et al. [5] are also reported for comparison.

	n	k
1 cycle	1.65	-13.36
5 cycles	0.80	-5.33
10 cycles	0.90	-5.33
69 % [5]	1.17	-8.62
85 % [5]	1.38	-9.50
94 % [5]	1.06	-6.92

3.2 Kinetics of recrystallization during annealing of ARBed Fe-36%Ni alloy

Fig. 5 presents the recrystallized volume fraction, *X*, versus annealing time deduced from the microhardness measurements using standard equation [14] (1):

$$X(t) = \frac{Hv_{\max} - Hv(t)}{Hv_{\max} - Hv_{\min}} \qquad (1)$$

Where *Hv(t)* stands for hardness value at time *t*, Hv_{max} is the maximum hardness of the as-severely deformed sample (at *t* = 0) and Hv_{min} is the minimum hardness of the fully recrystallized sample.

Zaefferer et al. [5] have published data on the kinetics of recrystallization of the same alloy after cold rolling and annealing at 600 °C, they are plotted together for comparison. It can be clearly seen that the 5 (ε = 4) and 10 (ε = 8) ARB samples kinetics are close to the 64 % (ε = 1.2) cold-rolled sample kinetics. For only the 1 ARB sample, kinetics are slower. The recrystallization of the Fe-36%Ni (wt. %) alloy sample after 5 ARB cycles occurs lately than for the cold rolled sample despite the closest equivalent strain (95 % thickness reduction, ε = 3.45). The explanation of these findings could be associated with the processing temperature. Indeed, material stores more energy during cold rolling than during hot ARB.

It can also be observed that after 300 sec, the recrystallization in the 5 ARB sample seems to be more effective than in the 10 ARB cycles. This finding is in line with the observation made by Beck et al. [15], who found that the grain boundary migration rate was slower in the specimen containing strips. In our case, the 10 ARB sample accumulated 1024 strips instead of 512 in the 5 ARB sample.

The kinetics of recrystallization could also be discussed using the Johnson-Mehl-Avrami-Kolmogorov (JMAK) relationship [16 – 18] (2) that gives the variation of the recrystallized fraction versus the annealing time:

$$X(t) = 1 - \exp(-kt^n) \tag{2}$$

Where X is the recrystallized fraction, t is the annealing time, k is temperature dependent and n is the Avrami time exponent. The n and k parameters can easy been obtained from the linearization of the JMAK equation. Table 1 presents the n and k values obtained for 1, 5 and 10 ARB samples. Results from Zaefferer et al. [5] are also reported in Table 1 for comparison.

It can be seen from Table 1 that the values of the Avrami time exponent n are around 1 for all samples which indicates the presence of heterogeneous site saturated nucleation of recrystallized grains [19]. The n values obtained in this study are slightly different from those calculated from data of Zaefferer et al. [5]. This difference may be due to the processing conditions that influence the kinetics of the recrystallization. Indeed, the data of Zaefferer et al. [5] were obtained for a cold rolled and annealing samples at 600 °C while in the present study, they were deduced for hot ARBed samples (at 550 °C) and annealed at 600 °C.

3.3 Texture evolution after annealing of ARBed Fe-36%Ni alloy

Fig. 6 shows the calculated ODF sections at φ2 = 0, 45 and 65° of Fe-36%Ni (wt. %) alloy after ARB processing for 1, 5, 10 cycles and annealing at 600°C for 120, 600 and 3600 sec. The location of ideal orientations is also indicated on the ODF sections. The main ideal texture components positions of FCC alloys and their descriptions are given in Table 2. As already reported by Tirsatine et al. [2], the texture of as deformed samples showed the presence of FCC dominant rolling texture components (Copper, S and Brass). Those components with a certain grain orientation distribution affect material proprieties during the thermomechanical treatment, yielding valuable information on them properties. It is worth noting that the texture of the samples after 1, 5 and 10 ARB cycles and annealing at 600 °C for 120 sec looks similar to that prior to annealing (presented in Reference [2]). With increasing annealing time, a more or less sharpening of Cube component accompanied by gradual decrease of Copper, S and Brass components are depicted. The variation of Cube fraction as function of annealing time in 1, 5 and 10 ARB samples is shown in Fig. 7.

After one hour annealing at 600 °C of 1 ARB sample, the Copper, S and Brass deformation texture components remain present. There is also a small amount of Cube retained from the initial state of the alloy (before deformation) [2]. Figs. 6 and 7 confirm indubitably that annealing of the 1 ARB cycle did not affect totally the deformation texture components that exhibited a sort of stability even after 3600 sec. At low deformation straining, the texture is retained because all the texture components may nucleate. Moreover, the texture tended to be isotropic because the twining might operate for all he texture components and hence generated new orientations. The global weakening of the texture should be ascribed to the occurrence of multiple twinning as discussed by [20]. This multiple twinning has already been observed in Al and Cu monocrystals and did not lead to a random texture but rather to a noticeable failing of the texture.

Annealing the samples after 5 and 10 ARB cycles modifies the texture components

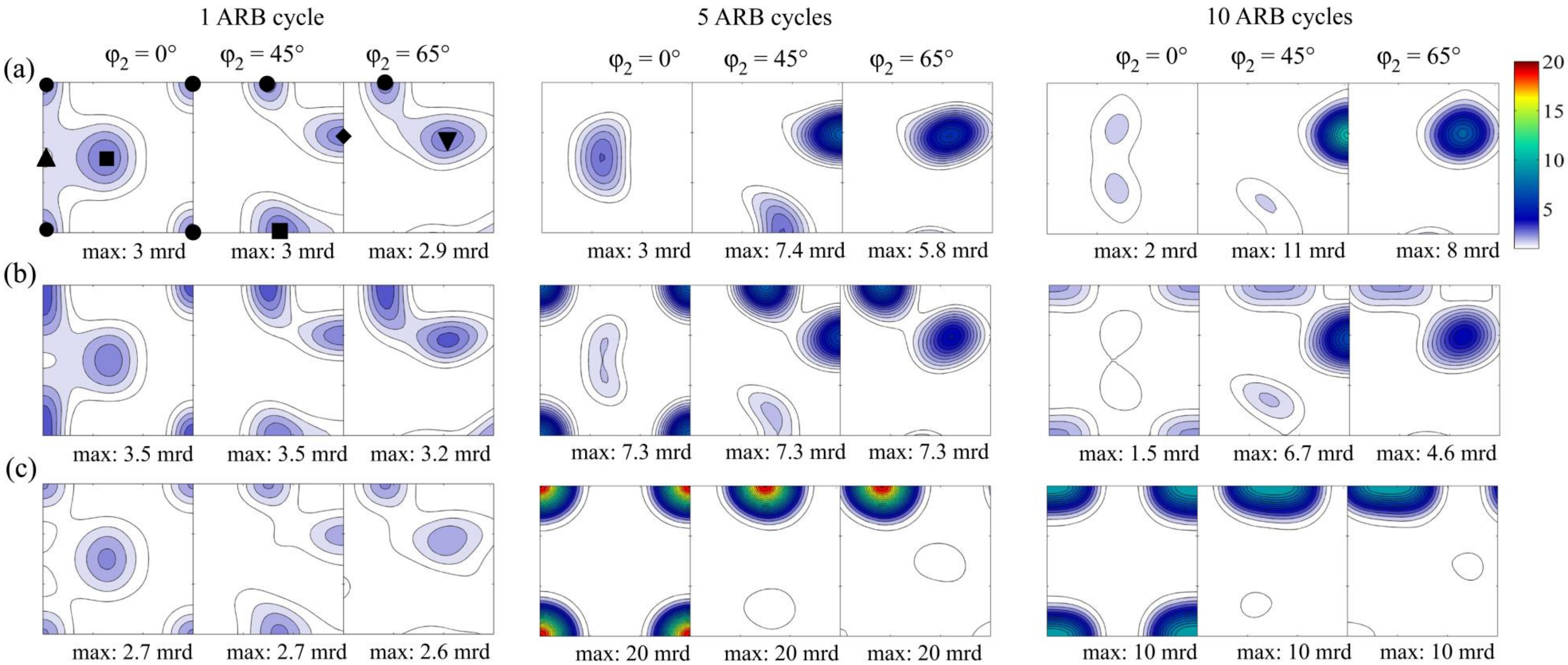

Fig. 6. ODF sections at φ2= 0, 45 and 65 ° of the Fe-36%Ni (wt. %) alloy after ARB processing and annealing at 600 °C for: (a) 120 sec, (b) 600 sec and (c) 3600 sec.
(full colour version available online)

Table 2

Main ideal rolling texture components of FCC alloys.

	Component	{hkl}<uvw>	Euler Angle φ_1	Euler Angle φ	Euler Angle φ_2
■	Brass	{110}<112>	35°	35°	45°
▲	Goss	{110}<001>	0°	45°	0°
●	Cube	{001}<100>	0°	0°	0°
◆	Copper	{112}<111>	90°	35°	45°
▼	*S*	{231}<346>	59°	29°	63°

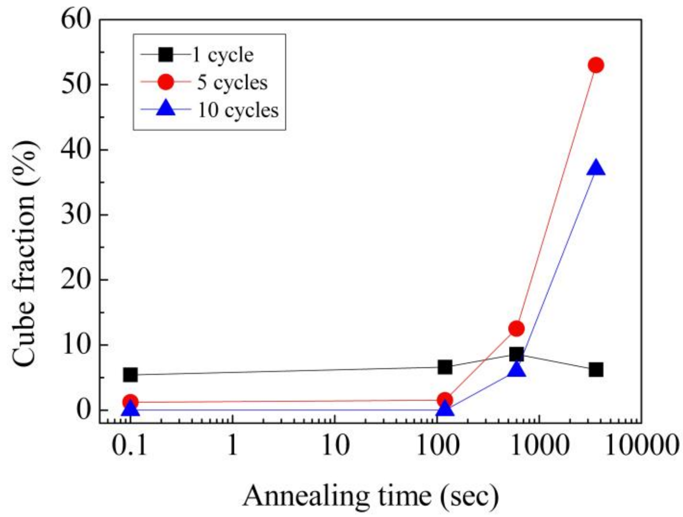

Fig. 7. Cube fraction in Fe-36%Ni (wt. %) alloy after ARB processing and annealing at 600 °C up to 3600 sec: (a) 1 ARB cycle, (b) 5 ARB cycles and (c) 10 ARB cycles.
(full colour version available online)

volume fractions and shows an overall decrease of the Copper, S, Brass deformation texture components and a net increase of the Cube component. The development of the Cube texture after conventional cold and hot deformation has been well studied in Fe-Ni system [21–23]. It is worth noting that annealing of samples after 5 and 10 ARB cycles leads to the development of a weak (with volume fraction ranging between 5 % and 2.5 %), Twin Cube (122)<221> (45°, 70.53°, 45°) component as can be seen in Fig. 6. **It is to be noted that this component did not exist in the deformed material but developed during the recrystallization annealing.**

Extensive observations by means of X-ray texture measurements and transmission electron microscopy (TEM) observations, including orientation measurement, of first stages of recrystallization were performed by [5, 20] in cold-rolled Fe-36%Ni alloy. Three deformation-induced heterogeneities that are lamella bands (LB), cube bands (CB) and shear bands (SB) were analyzed in relation to cube texture development. It has been explicitly shown that LB and SB did not play any role in recrystallization nucleation or texture formation. The CB were very appropriate for the nucleation of cube grains owing to their high orientation gradient, high misorientation across the band and well recovered cells [5, 20]. Since the texture evolution and kinetics of recrystallization of Fe-36%Ni alloy after processing by ARB (present study) and cold rolling [5, 20] are quiet close, it can be assumed that the same mechanisms of cube grain formation and evolution may operate.

After annealing for 600 sec, the Cube volume fraction in 5 ARB cycles is around 12 % but in the 10 ARB cycles it is just 6 %. This anomalous effect has already been reported in pure Cu processed by ARB and annealed at 150 °C up to 600 min [10]. These authors have reported the existence of large amount of small recrystallized grains formed around the bonded interfaces and having several different orientations (similar observations are reported in Fig. 1). These small grains were considered hence as principal weakening factor of the Cube texture development. These interfaces were previously wire-brushed which can induce a local area of severe plastic deformation, an origin of submicronic grain creation as for example in SMATed alloys [24]. These small grains contain low energy and have the same probability as Cube grains to nucleate. As the interface number increases, from 5 to 10 ARB cycles, the random nucleation increases and leads to a decrease of the Cube fraction. This texture dispersion can be verified during the first step of recrystallization (600 sec) and persists up to the final recrystallization (50 % and 35 % Cube fraction for 5 and 10 ARB cycles respectively).

To sum up, the ARB process does not allow developing a sharp Cube texture contrarily to what was obtained after high cold-rolling and annealing knowing that this sharp texture is often desired for superconductor applications [25]. An attempt to perform the ARB process at lower temperatures could permit increasing this Cube fraction. It remains to be checked whether a lower temperature could limit the grain growth. Moreover, it could be interesting to increase the ARB cycle number to increase the severe plastic deformation and then the nuclei number, in order to decrease the grain size after complete recrystallization.

4. Conclusion

The microstructure and texture of Fe-36%Ni (wt.%) alloy severely deformed by ARB up to 10 cycles and annealed at 600 °C up 3600 sec has been investigated using EBSD, the main results are summarized below:

- The microstructure of Fe-36%Ni (wt.%) alloy was not stable during annealing at 600°C.
- The recrystallization kinetics and texture after Accumulative Roll Bonding were similar to those after conventional cold rolling. The Cube texture component dominated but with weaker intensity and volume fraction.
- The recrystallization kinetics was expressed by the Avrami time exponent around 1 for all samples. This value indicates heterogeneous site saturated nucleation of recrystallized grains.
- The decrease in Cube fraction between 5 and 10 ARB cycles was probably due to the presence of small grains at the wire-brushed interfaces induced by severe plastic deformation.

Acknowledgements

The authors wish to thank Pierre-Louis REYDET from APERAM-alloys Imphy Society, France, for kindly providing the Fe-36%Ni (wt. %) alloy. This work was supported in part by the TASSILI program No. 12MDU862 / EGIDE: 26481WM.

References

[1] A. Azushima, R. Kopp, A. Korhonen, D.Y. Yang, F. Micari, G.D. Lahoti, P. Groche, J. Yanagimoto, N. Tsuji, A. Rosochowski, A. Yanagida CIRP: Annals-Manufacturing Technology 57 (2008) 716–735.

[2] K. Tirsatine, H. Azzeddine, T. Baudin, A.L. Helbert, F. Brisset, B. Alili, D. Bradai: J. Alloys Compd. 610 (2014) 352–360.

[3] N. Kamikawa, T. Sakai, N. Tsuji: Acta Materialia 55(17) (2007) 5873–5888.

[4] N. Tsuji, H. Takebayashi, T. Takiguehi, K. Tsuzaki, T. Maki: Acta Metall. Mater. 43 (1995)743–754.

[5] S. Zaefferer, T. Baudin, R. Pennelle: Acta mater. 49(6) (2001) 1105–1122.

[6] S. Chhann, D. Solas, A.L. Etter, R. Pennelle,

T. Baudin: Mater. Sci. Forum 550 (2007) 551-556.

[7] N. Tsuji, H. Takebayashi, T. Takiguchi, K. Tsuzaki and T. Maki: Acta Metallurgica et Materialia, 43 (1995) 755–768.

[8] B.L. Li, N. Tsuji, N. Kamikawa: Mater. Sci. Eng. A 423(1-2) (2006) 331–342.

[9] F. Bachmann, R. Hielscher, H. Schaeben: Solid. State. Phenom. 160 (2010) 63–68.

[10] N. Takata, K. Yamada, K. Ikeda, F. Yoshida, H. Nakashima, N. Tsuji: Mater. Trans. 48(8) (2007) 2043–2048.

[11] M. Cieslar, M. Poková: Materials 7 (2014) 8058–8069.

[12] Z. Guo, D. Solas, A.L. Etter, T. Baudin, R. Penelle: Mater. Sci. Forum 426–432 (2003) 2723–2728.

[13] W. Wang, F. Brisset, A.L. Helbert, D. Solas, I. Drouelle, M.H. Mathon, T. Baudin: Mater. Sci. Eng. A, 589 (2014) 112–118.

[14] O. R. Myhr, O.Grong: Acta Metall. Mater. 39(11) (1991) 2693–2702.

[15] P.A. Beck, J.C. Kremer, L.J. Demer: Transaction of American Institute of Mining, Metallurgical, and Petroleum Engineers 175 (1948) 372.

[16] A.N. Kolmogorov: Akad. Nauk. USSR Izv. Ser. Mat. 1(3) (1937) 355–359.

[17] W.A. Johnson, R.F. Mehl: Trans. Metall. Soc. AIME 135 (1939) 416–458.

[18] M. Avrami: J. Chem. Phys. 7 (1939) 1103–1112.

[19] J.W. Christian: The Theory of Transformations in Metals and Alloys: Advanced Textbook in Physical Metallurgy, second ed., Peramon Press, Oxford, 1975.

[20] F. Julliard: Study of Recrystallization Mechanisms in Invar alloy, Ph.D Thesis, Université Paris Sud, Orsay, France (2001).

[21] R. Penelle, T. Baudin: Adv. Eng. Mater. 12(10) (2010) 1047–1052.

[22] V. Branger, M. H. Mathon, T. Baudin, R. Penelle: Scripta Mater. 43(4) (2000) 325–330.

[23] F. Caleyo, T. Baudin, R. Penelle, V. Venegas: Scripta Mater. 45(4) (2001) 413–420.

[24] G. Proust, D. Retraint, M. Chemkhi, A. Roos, C. Demangel: Microsc Microanal 21(4) (2015) 919–926.

[25] Y. Ateba Betanda, A.L. Helbert, F. Brisset, M. Wehbi, M.H. Mathon, T. Waeckerlé, T. Baudin: Adv. Eng. Mater. 16(7) (2014) 933–939.